Numerical study of mobilized friction along embedded catenary mooring chains

Sun, C., Feng, X., Neubecker, S.R., Randolph, M.F., Bransby, M.F., Gourvenec, S.

ABSTRACT

Understanding the soil resistance along an embedded anchor chain is imperative for efficient and economic design of an overall mooring system as it determines the magnitude and direction of the load at the padeye of the anchor. The tensioning process of an embedded chain for catenary moorings was modeled using a coupled Eulerian–Lagrangian (CEL) finite element approach simulating the large deformations of the chain as it cuts through the soil to form an inverse catenary. The analyses reveal that the configuration of the embedded chain and the relationship between tension and chain angle at the padeye show excellent agreement with previously published analytical predictions. However, the ratio of the tension at the padeye to that at the mudline obtained from CEL is significantly higher than the theoretical values, mainly due to partial mobilization of the frictional soil resistance along the length of the chain. The CEL results indicate that the partial mobilization is a result of the combined-loading effect during failure of the soil around the embedded chain as it cuts through the seabed, in contrast with the conventional assumption that the ultimate frictional and normal soil resistances are mobilized simultaneously. A new design approach is proposed for calculating the local equivalent coefficient of friction based on the yield locus for a deeply embedded chain and the normality rule.

Keywords: Anchor chain; catenary mooring; chain-soil interaction; coupled Eulerian–Lagrangian; finite element analysis

No. of words (without abstract and references):	5917
No. of tables:	0
No. of figures:	16

[1]Chao SUN
Centre for Offshore Foundation Systems
Oceans Graduate School
University of Western Australia
35 Stirling Highway, Crawley
Perth, WA 6009
Australia
Tel: +61 4 6974 3231
Fax: +61 8 6488 1044
Email: chao.sun@research.uwa.edu.au

[2]Xiaowei FENG, Ph.D.
Centre for Offshore Foundation Systems
Oceans Graduate School
University of Western Australia
35 Stirling Highway, Crawley
Perth, WA 6009
Australia
Email: xiaowei.feng@uwa.edu.au

[3]Steven R. NEUBECKER, Ph.D.
Centre for Offshore Foundation Systems
Oceans Graduate School
University of Western Australia
35 Stirling Highway, Crawley
Perth, WA 6009
Australia
Email: steven.neubecker@uwa.edu.au

[4]Mark F. RANDOLPH, Ph.D.
Centre for Offshore Foundation Systems
Oceans Graduate School
University of Western Australia
35 Stirling Highway, Crawley
Perth, WA 6009
Australia
Email: mark.randolph@uwa.edu.au

[5]Mark Fraser BRANSBY, Ph.D.
Centre for Offshore Foundation Systems
Oceans Graduate School
University of Western Australia
35 Stirling Highway, Crawley
Perth, WA 6009
Australia
Email: fraser.bransby@uwa.edu.au

[6]**Susan GOURVENEC, Ph.D.**
School of Engineering
Faculty of Engineering and Physical Sciences
University of Southampton, Southampton, UK
Email: Susan.Gourvenec@southampton.ac.uk

INTRODUCTION

Buoyant offshore structures, which provide a variety of functions across the offshore sector, require a mooring system and anchor to keep station. Offshore anchors vary in configuration and operational mode but all generally have a mooring line attachment point, or padeye, below the mudline, with a section of the chain embedded in the soil (Randolph and Gourvenec 2011). For a catenary mooring line applying a horizontal load at the seabed, the embedded chain will form an 'inverse catenary' in the soil to maintain equilibrium between the chain tension and the soil resistance. Quantifying the normal and frictional soil resistances to the chain is required to calculate the configuration and tension profile of an embedded chain, enabling efficient anchor design according to the magnitude and inclination of the load at the padeye.

Analytical solutions

System behavior:

Solutions for the behavior of the whole length of an embedded chain in undrained soil conditions were developed by discretizing the chain into a number of arc-shaped/curvilinear elements in mechanical equilibrium with transmitted tension and soil resistance and then incrementally integrating the equilibrium equations from one end of the chain to the other. Early work by Reese (1973) discretized a weightless embedded chain as a succession of arcs of circles with varying radii, without considering the effect of frictional soil resistance on axial chain movement. The solution was improved by adding the effects of chain weight and frictional soil resistance, leading to a significant reduction of the chain tension at the anchor (Gault and Cox 1974). Vivatrat et al. (1982) considered an embedded chain as a series of curvilinear segments establishing the pair of differential equations governing respectively the variation of chain tension and geometric configuration as

$$\frac{dT}{ds} = F + w_c \sin\theta \tag{1}$$

$$T\frac{d\theta}{ds} = -Q + w_c \cos\theta \tag{2}$$

where T is the tension in the chain acting over the incremental chain length ds, θ is the angle subtended by the chain to the horizontal, w_c is the submerged weight of chain per unit length, and Q and F are respectively the normal and frictional soil resistances per unit length. The chain configuration and equilibrium of an element is illustrated in Figure 1, with boundary conditions of T_a and θ_a at the padeye at depth z_a, leading to tension T_m and θ_m (taken as zero here) at mudline. In general, since for most moorings T_m and θ_m are specified, iteration is needed in order to establish compatible values of T_a and θ_a. The analysis basis for embedded chains proposed by Vivatrat et al. (1982) has since been adopted in many other studies (e.g. Degenkamp and Dutta 1989; Dutta and Degenkamp 1989; Neubecker and Randolph 1995a; Neubecker and Randolph 1995b; Neubecker and Randolph 1996).

The differential equations (Eqs. (1) and (2)) were solved in closed-form by neglecting the weight of the chain, resulting in the tension profile (Neubecker and Randolph 1995b)

$$\frac{T}{T_a} = e^{\mu(\theta_a - \theta)} \tag{3}$$

with the chain friction coefficient μ defined as the ratio F/Q.

The Neubecker & Randolph solution also established the variation of the chain angle as

$$\frac{T_a}{1+\mu^2}\left[e^{\mu(\theta_a-\theta)}(\cos\theta + \mu\sin\theta)\right]_{\theta}^{\theta_a} = \int_z^{z_a} Q dz \tag{4}$$

which may be simplified for small-angles as

121 $$\frac{T_a}{2}(\theta_a^2 - \theta^2) = \int_z^{z_a} Q dz \quad (5)$$

122 In all the above solutions, the soil resistances Q and F, normal and parallel to the chain axis,
123 have been assumed uncoupled and fully mobilized simultaneously to the corresponding
124 ultimate capacities Q_u and F_u.

125 ***Chain-soil forces:***

126 Chains comprise multiple separate links with alternating orientations to the chain axis (Figure
127 2a) and chains of bar diameter d_b having individual link geometries that are typically 5-6d_b long
128 and ~3.5d_b wide. Consequently, in order to calculate soil resistances for this complex geometry,
129 approximations about the geometry have been made by introducing an effective width of $E_n d_b$
130 for the normal resistance and effective perimeter $E_t d_b$ for frictional resistance (Reese 1973).

131 Under undrained conditions in soil with shear strength s_u, the ultimate normal resistance Q_u and
132 frictional resistance F_u may therefore be estimated (Degenkamp and Dutta 1989) as

133 $$Q_u = E_n d_b N_c s_u \quad (6)$$

134 $$F_u = E_t d_b s_u \quad (7)$$

135 where N_c is the bearing capacity factor. The apparent coefficient of friction μ may be deduced
136 from the effective width and the bearing capacity factors as $F_u/Q_u = E_t/(E_n N_c)$.

137 Proposed values of the effective width parameters, E_n and E_t, and the bearing capacity factor
138 N_c varies among researchers. The effective width of chain in bearing was first introduced by
139 Reese (1973), with an upper bound value of $E_n = 3$ proposed by assuming that no flow of soil
140 through the opening in the chain was permitted. Vivatrat et al. (1982) adopted the bearing area
141 per unit length as the average of the maximum and minimum values, considering different
142 orientations of the chain links with respect to the soil, and the tangential area as the surface area

of the chain link, proposing effective width parameters E_n = 2.6 and E_t = 10 for calculating the normal and frictional resistances per unit length, respectively. For the bearing capacity factor N_c, a value equal to the ultimate lateral bearing capacity factor at depth for a pile, ranging from 9 to 11, was proposed initially (Reese 1973; Vivatrat et al. 1982). Yen and Tofani (1984) suggested that E_n = 2.37 and E_t = 5.7 ~ 8.9 for stud-link chains based on a series of model tests, back-calculating values of N_c between 7.1 and 12.1. Degenkamp and Dutta (1989) quantified average values of E_n and E_t as 2.5 and 8.0 by investigating $6d_b$ stud-link and $5d_b$ studless chains with both orthogonal and diagonal configurations. The bearing factor N_c was assumed equivalent to that of a strip foundation, increasing with depth from 5.14 at mudline to a maximum of 7.6 (Degenkamp and Dutta 1989; Dutta and Degenkamp 1989; Neubecker and Randolph 1995a; Neubecker and Randolph 1995b; Neubecker and Randolph 1996). These result in values of μ between 0.4 and 0.6.

Experimental observations and numerical simulations of embedded anchor chains

Frankenmolen et al. (2016) reported centrifuge tests of chain-soil interaction for surface and embedded chains in carbonate sand. The chain configurations for the embedded chain under monotonic tensioning showed agreement with the analytical solutions set out in Eq. (2), except for cases where the chain formed a padeye angle greater than 70°. However, the back-calculated 'operative' coefficient of friction (i.e. derived from tensions and angles at the anchor and mudline using Eq. (3)) were significantly lower than obtained from the chain surface dragging tests. Partial mobilization of the frictional resistance along the embedded chain was considered one of the primary reasons.

Rocha et al. (2016) presented results of a series of chain tensioning laboratory tests in very soft clay (water contents of 100 to 120%), including cycling of the mudline load between zero and a fixed maximum value at various mudline chain angles. At each maximum load level the deduced coefficient of friction consistent with Eq. (3), lay in the approximate range 0.2 to 0.3.

Han and Liu (2017) proposed a global yield locus for an embedded chain on the basis of data from model tests on tensioning of an Omni-Max anchor in soft clay (s_u ~ 1.2 to 1.4 kPa). Mooring lines of both chain and rope were investigated and measured tensions at mudline and anchor padeye were used to evaluate equivalent friction coefficients on the basis of Eq. (3). Again, they showed that the deduced values of μ varied with progress of the test, decreasing from a high value initially to steady values in the range 0.2 to 0.3.

The experimental data discussed above challenge the conventional assumption in analytical methods that bearing and friction are mobilized simultaneously along the entire length of the chain. Explicit consideration of the bearing and shear components indicates that combined-loading effects may lead to reduced friction of the chain, resulting in operative friction coefficients that are significantly lower than might be estimated otherwise, for example with values from model tests in clay that are about 50% of the range suggested by Degenkamp and Dutta (1989).

Numerical investigations of the behavior of an embedded chain have been reported using the Coupled Eulerian-Lagrangian (CEL) method. Pre-tensioning of an anchor chain for the installation of a catenary mooring line has been examined (e.g. Kim et al. 2015; Zhao and Liu 2013; Zhao and Liu 2014; Zhao and Liu 2016), and the chain configuration and tension profiles of the embedded chain compared with existing analytical predictions. Although discrepancies between the results and the analytical tension profile of an embedded chain were noted, these were not interpreted systematically, inspiring the current investigation of the chain-soil interaction using CEL.

Scope of present study

This paper presents results of Coupled Eulerian-Lagrangian finite element analysis of the undrained response of an embedded chain in the orthogonal space of normal and frictional

resistances. The tensioning process of the chain is modelled with a fixed anchor point ('padeye') and a horizontally loaded chain at the seabed. The chain is tensioned from the vertical 'installed' position to an equilibrium state in an inverse catenary, with gradually decreasing padeye angle as the tension is increased. Geometric configurations and tension profiles from the numerical analyses are compared with analytical predictions using the (Neubecker and Randolph 1995b) approach. Investigations of the soil resistances mobilized along the chain are presented in a yield-locus context. A method for calculating the local equivalent coefficient of friction of the embedded chain is proposed with the chain configuration established using the Neubecker & Randolph solution and the yield locus derived from separate analyses for a deeply embedded chain. This is then extended to derive a formulation for estimating the global operative friction factor for the embedded chain system, taking account of the variation in mobilized friction along the chain length.

FINITE-ELEMENT MODEL

Modelling software and approach

All finite element analyses were carried out with the coupled Eulerian-Lagrangian (CEL) approach provided in the software Abaqus (Dassault Systèmes 2014). The basis of the CEL approach is that the element nodes move temporarily with the material during a Lagrangian calculation phase, which is followed by mapping to a spatially 'fixed' Eulerian mesh. This enables efficient simulation of large deformation problems, in this case the cutting of a mooring chain through a soil mass from an initially vertically position to form an inverse catenary.

Chain geometries

The chain was modelled as a line of equally spaced, rigid cylindrical segments, connected using 'LINK' connector elements provided as standard in Abaqus (Figure 2a). The LINK connectors

transmit axial force but no bending moment, and maintain a fixed distance between the two connected nodes.

The length l_s and the diameter d_s of each segment, and the space between adjacent segments, s_s are the three geometric variables governing the dimensions of the model chain. In the current analyses, l_s was taken as 1 m, with s_s and d_s being 0.1 m and 0.25 m respectively.

The geometries of chain in the CEL model were selected to model a standard $5d_b$ studless chain as shown in Figure 2a. Each link pair of the $5d_b$ studless chain was represented by one bar segment together with one spacing, i.e. the sum of l_s and s_s was equivalent to the length of one link pair ($6d_b$). For this model, $l_s + s_s = 6d_b = 1.1$ m, giving $d_b \sim 0.18$ m. This provides a way to relate d_s with d_b (i.e. $d_s/d_b = 0.25/0.18$ for this model) for the interpretation of the resistances obtained from the CEL modelling. A detailed calibration exercise is presented later in order to evaluate the numerical limiting normal and frictional resistances of the simulated chain, together with a yield locus.

The embedded chain model comprised 49 segments (giving a total length of 53.9 m) as shown in Figure 2b. The padeye was set (arbitrarily) to 9 m below the soil surface, providing sufficient embedment to investigate the chain tensioning in a realistic manner without introducing unnecessary length (and therefore computational expense). Two chain weights of $w_c = 0$ (weightless chain) and 1.5 kN/m were considered and the chain was loaded horizontally at the seabed (i.e. as a catenary mooring).

Soil domain

The soil was assumed to be fully undrained during the chain tensioning process and consequently total stress analyses were performed. The undrained soil strength was assumed to increase linearly with depth z, according to $s_u = 2 + 1.2z$ kPa, with the effective soil weight being 2.4 kN/m^3. These values are typical of deepwater seabed sediments offshore West Africa

(Ehlers et al. 2005), which have been the focus of significant attention recently following observations of anchor line trenching (Bhattacharjee et al. 2014; Colliat et al. 2018). A linear elastic-perfectly plastic constitutive model, obeying the Tresca failure criterion, was adopted for the soil. The Young's modulus E was taken as $500s_u$ and Poisson's ratio as 0.49 to approximate incompressible soil response for undrained conditions. The regular mesh comprised 8-noded linear brick elements with reduced integration (EC3D8R in the Abaqus element library). A central fine mesh zone (minimum mesh size L_e = $0.35d_s$) was used to discretize the soil-flow area where significant soil distortion was expected due to the changing chain configuration during tensioning.

CEL model setup

Figure 2b presents the global view of the CEL model (top) with the detailed chain model illustrated at the bottom of the figure. Only half of the anchor chain (with a semi-circular cross-section) and soil domain was analyzed because of symmetry with respect to the vertical plane through the chain axis. As shown in Figure 2b, the left boundary and base of the soil domain extended $7.5l_s$ (7.5 m) from the padeye. The length of the whole soil domain was taken as 67.6 m, and the out-of-plane thickness as $30d_s$ (7.5 m) to avoid boundary effects. Above the soil surface, a layer of 'void' with height $1l_s$ (1 m) was prescribed, sufficient to accommodate soil heave in front of the chain during tensioning.

The anchor chain was initially 'wished-in-place' in the post-installation configuration with a vertical section fully embedded and attached to the padeye, and a horizontal section laid on the seabed with the centerline of the chain level with the seabed surface. Subsequently, the motion of the dragging point was activated by applying a constant horizontal velocity v_d, forcing the chain to cut gradually through the soil. The dragging point was displaced horizontally until the final padeye inclination angle θ_a reached 35° to the horizontal with the dragging point located sufficiently far away from the padeye to ensure that the chain remained horizontal at the

dragging point. The response of two segments (#13 and #25, highlighted and numbered on Figure 2b) was examined in post-processing to understand the chain behavior in detail.

The local coefficient of friction of the chain-soil interface was taken as 0.5 times the normal force using the 'penalty' contact option in the Abaqus library. A quasi-static solution for the tensioning process of the chain was achieved through a parametric sensitivity study of the combination of mesh density, loading velocity and coefficient of friction of the interface. Justification for the selection of a linear computational loading velocity (of v_d = 4.0e-5L_e = 1.4*e-5*d_s per increment, equivalent to a velocity of 0.05 m/s) is shown below.

Validation of the CEL model

Prior to analyzing the embedded chain for a catenary mooring, a straight seven-segment chain was embedded horizontally at a depth of 18d_s (4.5 m) and then displaced in normal and axial directions. Comparisons of the normal and frictional soil resistances with those estimated using Eqs. (6) and (7) allowed verification of the CEL modelling, including the soil properties, chain size, interface properties, boundaries, mesh refinement and simulation velocities, consistent with those adopted in the global embedded chain model. Resultant loads on the outer two segments were excluded in the interpretation, avoiding end effects from the two ends of the seven-segment section.

A series of analyses were conducted using different input velocities (8.0 x 10^{-6}, 4.0 x 10^{-5}, 2.0 x 10^{-4} and 1.0 x 10^{-3} L_e per time increment) were conducted to quantify how the ultimate normal and frictional capacities per unit length changed with velocity due to numerical errors and therefore help select the simulation velocity. The normalized normal and frictional resistances $N_b = F_{N,\,sum}/Ld_bs_u$ and $N_s = F_{S,\,sum}/Ld_bs_u$ are shown in Figure 3, where $F_{N,\,sum}$ and $F_{S,\,sum}$ are respectively the sums of the normal and frictional soil resistance forces on the five central

segments of the chain, while L corresponds to the total length of the central five links, i.e. $5(l_s + s_s)$ and s_u is the undrained strength at the depth of the chain element centroid.

Pursuing a completely convergent solution would require use of an extremely small velocity, as observed in CEL analysis of cone penetration by Wang et al. (2015), which would preclude its use in the large-domain full chain system analyses. However, the CEL results of normal and frictional capacities were comparable with the estimated values derived from Eqs. (6) and (7) using the values of $N_c = 7.6$, $E_n = 2.5$ and $E_t = 8$ values recommended by Degenkamp and Dutta (1989). Closest agreement was obtained for the loading velocity of $4.0 \times 10^{-5} L_e$ per increment and so that simulation velocity was selected for the full-chain simulations (Figure 3).

Overall, the adopted simulation velocity resulted in an ultimate normal resistance value of $N_{b,\,ult} = Q_{u,\,deep}/d_b s_u = 19$ (equal to the Degenkamp and Dutta (1989) recommendation), and ultimate frictional resistance $N_{s,\,ult} = F_{u,\,deep}/d_b s_u = 6.5$ (compared to 8 from Degenkamp and Dutta (1989)). This results in an acceptable equivalent 'friction coefficient' μ_p ($= F_{u,\,deep}/Q_{u,\,deep} = 0.34$), towards the lower end of the range of 0.4 – 0.6 discussed earlier.

The adopted simulation velocity is about the lowest practical, given that analysis of the full chain system still required about 350 hours on a fast server. For internal consistency, all later simulations were performed applying this velocity at the chain end. While there will still be some velocity variation at different locations along the chain, the variation of the net friction coefficient is relatively minor and will not affect the validity of the conclusions reached.

RESULTS

Yield loci for embedded chain segments

The normal and tangential motion of the embedded chain induces failure of the soil as it cuts through. Consequently, before analyzing the complete chain system, a suite of numerical

analyses were performed on the seven-segment section of chain (weightless and w_c = 1.5 kN/m) for a deeply embedded (centroid depth = 18d_s (4.5 m, s_u = 7.4 kPa)) and a surface-laid chain condition (centroid depth = 0 m (s_u = 2.0 kPa)). These analyses were designed to examine how the normal and frictional soil resistances interact and to develop yield loci.

The resulting interaction diagrams are shown in terms of normalized normal and frictional resistances N_b and N_s in Figure 4 for the two different embedment conditions. To probe the yield locus for the deep condition, displacement-controlled probes (each at a different displacement angle ω to the normal of the chain axis) were conducted (Figure 4a). A yield locus was then selected, based on the final load path sections (when the load path reaches the failure envelope and turns tangential to it) and the final points of the load paths when loads had stabilized with further displacement. The yield locus took the form of a generalized ellipse:

$$\left(\frac{N_b}{N_{b,ult}}\right)^m + \left(\frac{N_s}{N_{s,ult}}\right)^n = 1 \tag{8}$$

where $N_{b,\,ult}$ and $N_{s,\,ult}$ are taken as 19 and 6.5 for pure penetration and sliding (see Figure 4a) and m and n are fitting parameters. The exponents m and n of the yield locus function were selected as 2.0 and 2.3, which are close to those proposed by Han and Liu (2017). Furthermore, separate analyses revealed that the shape factors m and n remain consistent for different gradients of the soil shear strength. Also from Figure 4a, normality is shown to apply for the yield locus of the deeply embedded section, with the plastic displacement ratio of the chain consistent with the gradient of the yield locus. In this way, the resistance ratio F/Q during failure of the soil around the chain is related to the kinematics of the chain.

Although the above envelope does not fit the numerical data perfectly (for example, it cannot capture discontinuous changes in mechanisms around the envelope), it is simple and easily implementable in design. Given that each point along the chain is at a different point on the

envelope, this is likely to mean that minor disparities are insignificant, and consequently, we consider that the approach is sufficiently accurate for design purposes.

For the surficial chain segments, it was found difficult to probe the yield locus with a displacement-controlled scheme. Instead, the *Q-F* yield locus was deduced using load-controlled analyses. The load paths are shown in Figure 4b with the final point on each line representing 'failure' (i.e. a point where increasing displacement does not change the mobilized resistance). The resulting envelope is a chili-leaf-shaped locus, with no frictional resistance when the normal force is zero because the chain is weightless. The shape of the locus near the original reflects the contact with a frictional coefficient of 0.5 adopted in the CEL model for the chain-soil contact interface.

A comparison between the yield loci for w_c = 0 and 1.5 kN/m is presented in Figure 5. The difference between the normal capacities of the weightless and weighty chains is simply $w_c/d_b s_u$. Both yield loci show greater interaction effects than those for a suction caisson (Aubeny et al. 2003).

Global chain analyses

Figure 6 presents the development of padeye angle θ_a and tensions at mudline T_m and padeye T_a as the chain is dragged. The padeye angle remained at 90° until a significant displacement, approximately 3.5 m, was imposed at the dragging point, and then decreased almost linearly as the dragging distance increased to the target 6.4 m. The delay in change of θ_a reflects the gradually developing catenary profile, with parts of the chain at shallow depth cutting through the soil much earlier than the chain near the attachment point. The tensions develop linearly initially, but with a gradually increasing rate as the chain becomes taut. Minimal chain-weight effect is shown when comparing the results of weightless and weighty chains, apart from slight divergence of the tension responses at a large dragging distance.

The relationships between padeye angle and chain tension are shown in Figure 7, comparing the results with the analytical solutions of Neubecker & Randolph (1995b). Although good agreement is evident for the response at the anchor padeye (T_a-θ_a), the analytical solutions indicate higher values of T_m for a given padeye angle than obtained from the CEL analyses. This is discussed in more detail later.

Figure 8 compares the configurations of the embedded chain obtained from the CEL analyses for selected chain inclination angles at the padeye (θ_a) during the tensioning process. The CEL results of the chain profiles agree well with the analytical predictions derived from Eq. (4) with $Q = Q_{u,\,deep} = 19 d_b s_u$ and $\mu = \mu_p = 0.34$, indicating the robustness of the Neubecker & Randolph relationships. It appears reasonable to use $Q_{u,\,deep}$ at all depths in Eq. (4) rather than adjust it to allow for the decrease at shallow embedment. This reflects the small contribution of resistance for the shallowly embedded part of the chain compared with the integrated resistance of the whole chain. The additional embedment due to the chain weight is minimal in proximity to the mudline (Figure 8b), reflecting the relatively low self-weight generated bearing pressure of the chain ($w_c/d_b s_u = 4.2$ for the mudline shear strength of 2 kPa) compared with a limiting bearing factor of over 12 (see Figure 4b).

The CEL results of the tension ratio T_a/T_m as a function of the decreasing padeye angle are compared with analytical predictions in Figure 9a for the weightless chain. A gradual increase of the tension ratio with increasing θ_a is shown for both CEL results and the Neubecker & Randolph predictions by Eq. (3). However, the tension ratio obtained from the CEL analysis is significantly higher than the predictions by Eq. (3), e.g. CEL gives $T_a/T_m = 0.90$ for $\theta_a = 75°$, compared with 0.65 by Eq. (3) (Figure 9a).

The depth profiles of normalized tension T/T_a in the chain are shown in Figure 9b for the final padeye angle of $\theta_a = 35°$ and chain weights of $w_c = 0$ and 1.5 kN/m. The CEL results show

much smaller exponential increases with distance from the padeye compared with the analytical predictions consistent with the increased T_a/T_m ratios discussed above.

To globally re-evaluate the 'operative' coefficient of friction over the full length of the embedded chain by Eq. (3), the CEL results of the tension ratio T_a/T_m as a function of the dragging distance are compared in Figure 10 against the analytical predictions derived based on the padeye angle-dragging distance relationships (Figure 6a) and Eq. (3) with varying 'operative' coefficient of friction μ values. Full mobilization of the (uncoupled) frictional resistance corresponds to the case of $\mu = \mu_p = 0.34$. In contrast, the CEL T_a/T_m results agreed with the analyses using $\mu = 0.07$, indicating that only about 20% on average of the potential frictional capacity is mobilized along the embedded chain during the tensioning process. Note that the operative coefficient of friction back-figured from the T_a/T_m profile does not affect agreement of the CEL and Neubecker-Randolph T_a-θ_a responses (see Figure 7) since Eq. (5) indicates that the chain tension at the padeye, T_a, is insensitive to the mobilized frictional resistance.

The operative coefficient of friction provides a straightforward assessment of the partial mobilization of the frictional resistance, even though it cannot rigorously define the mobilized frictional resistance for each given anchor chain segment. This will be examined in the next section.

Mobilized soil resistance along the anchor chain

The evolution of normalized normal and frictional soil resistances, $Q/Q_{u,\,deep}$ and $F/F_{u,\,deep}$ for two representative segments (identified as 'segment #13' and 'segment #25') in the weightless chain during tensioning is shown in Figure 11. The mobilized frictional and bearing forces for these elements are compared with the yield loci derived for the surficial and deeply embedded

chain for chain profiles (1), (2), (3) and (4), which correspond to dragging distances of 1.5, 3.0, 4.5 and 6.0 m respectively.

The evolution of the soil resistances reflects the cutting through of the chain during the tensioning process. Both segments initially slide (axially) across the seabed, with the data points for normal and tangential resistances travelling along the low Q/Q_u segment of the locus for the surficial chain. Subsequently, the *Q*-*F* states transition between the yield locus for the surficial chain and that for the deeply embedded section, corresponding to the soil failure at intermediate depths as the chain cuts progressively deeper into the soil. Finally, the *Q*-*F* loading condition on each chain segment moves towards a pure bearing condition, i.e. $Q \sim Q_{u,\,deep}$, and $F \sim 0$, as the chain is tensioned.

The normalized normal and frictional soil resistances derived from CEL for all chain segments at the mudline (z = 0), at intermediate depths (z = 0 to $3d_s$) and when deep (z = $3d_s$ to z_a) are plotted in Figure 12 against the yield loci for surficial and deeply embedded chains at padeye angles of θ_a = 75°, 60°, 45° and 35°. It is evident that the *Q*-*F* data for the segments embedded at depths from $3d_s$ (0.75 m) to z_a (9 m) lie close to the outer (deep embedment) yield locus, while those for the surficial segments lie close to the inner (surficial) locus, with some transition segments in between those two groups.

For the segments at the mudline, the operative *F*/*Q* ratios (i.e. μ in analytical equations) lie just above the line of μ_p, showing 'sliding' behavior. For the deeply embedded sections, normal resistance is close to fully mobilized ($Q \sim Q_{u,\,deep}$), while frictional forces are small ($F \sim 0$), so that the friction ratio *F*/*Q* is considerably smaller than μ_p. This is attributed to the dominance of normal movement, rather than axial movement, which is restricted by the padeye and the axial stiffness of the chain. Due to the relatively small value of *Q* near the soil surface, the global operative coefficient of friction is dominated by the *F*/*Q* ratios for the deeply embedded part of the chain.

As the tensioning proceeds, the operative coefficient of friction obtained from the CEL analyses may be expected to reduce as an increasing length of chain cuts through the soil to become fully embedded, mobilizing a greater proportion of the full bearing resistance. This cannot be captured rigorously by a simple constant coefficient of friction, even though a value of $\mu = 0.07$ gives a reasonable fit to the overall behavior (Figure 10).Method for calculation of the equivalent frictional coefficient

The *Q*-*F* yield locus for the deeply embedded chain sections may be used as the basis for an analytical approach to determine the *F*/*Q* ratio at each point along the embedded chain as a function of embedment depth and the chain angle. In this section, a method is proposed based on the chain configurations predicted by the Neubecker-Randolph solution.

The schematic of the yield locus is illustrated in Figure 13 together with the plastic potential. The normality rule was adopted appropriate for deep undrained conditions (e.g. Bransby and Randolph 1998; O'Neill et al. 2003) and based on the evidence shown in Figure 11. The incremental (plastic) displacement normal and tangential to each chain segment defines the plastic flow vector, i.e. $\tan\omega = \Delta u_t/\Delta u_n$, during the cutting through of the chain. Therefore, the local equivalent coefficient of friction, μ_{le} in Figure 13, can be determined by

$$\mu_{le} = \frac{F_{deep}}{Q_{deep}} = \frac{N_s}{N_b} = \left[\frac{m}{n}\left(\frac{N_{s,ult}}{N_{b,ult}}\right)^n \tan\omega\right]^{1/(n-1)} = \left[\frac{m}{n}\left(\frac{N_{s,ult}}{N_{b,ult}}\right)^n \frac{\Delta u_t}{\Delta u_n}\right]^{1/(n-1)} \quad (9)$$

and assuming (for simplicity) that the normal resistance is fully mobilized ($Q_{deep} = Q_{u,\,deep}$). Separate analyses were performed with the value of Q_{deep} derived rigorously according to the yield locus. However, it was found for the cases considered here that this made no significant difference to the results compared with assuming $Q_{deep} = Q_{u,deep}$. The equation can be modified to allow for the chain weight and the chain inclination as

$$\mu_{le} = \left[\frac{m}{n} \left(\frac{N_{s,ult} + w_c \sin\theta \big/ d_b s_u}{N_{b,ult} - w_c \cos\theta \big/ d_b s_u} \right)^n \frac{\Delta u_t}{\Delta u_n} \right]^{1/(n-1)} \quad (10)$$

The relationship between μ_{le} and $\Delta u_t/\Delta u_n$ is therefore determined by Eqs. (9) and (10) with the shape parameters m and n of the yield locus for the deeply embedded chain and the resistance factors $N_{s,\,ult}$ and $N_{b,\,ult}$ already known.

The above equations can be used to analyze the response of the chain system in the soil as follows:

Step 1: Estimate the configuration of an embedded chain for a given padeye angle θ_a using the Neubecker and Randolph (1995b) solution (Eq. (4)) with $\mu = \mu_p = F_{u,\,deep}/Q_{u,\,deep}$.

Step 2: Update the configuration by applying a small incremental change of the padeye angle (e.g. $\Delta\theta_a = 1.0 \times 10^{-8}$ rad) using the parameters from the previous step.

Step 3: Calculate the incremental displacement in the normal and tangential direction for each individual chain element along the embedded chain.

Step 4: Calculate μ_{le} for each chain element using Eq. (9) or (10).

Step 5: Calcualte the updated mudline load and anchor padeye loads using the updated μ values.

Step 6: Return to step 2 and loop until the final design mudline load (or a target padeye chain angle) is reached.

The values of $\Delta u_t/\Delta u_n$ and μ_{le} calculated from Eq.(9) are shown on Figure 14 as a fuction of the embedment depth for selected configurations of an embedded chain with padeye angles θ_a = 75°, 60°, 45° and 35°. The incremental displacement ratio $\Delta u_t/\Delta u_n$ at given depth z/z_a decreases as padeye angle θ_a decreases (Figure 14(a)), reflecting a reduction of the tangential motion of

471 the chain as it is tensioned. For a given padeye angle, there is a rapid increase of $\tan\omega$ from the
472 padeye to the mudline, because of the relaxation of the axial movement constraint when remote
473 from the padeye. Similar to the trend of $\Delta u_t/\Delta u_n$ shown in Figure 14(a), μ_{le} decreases as the
474 padeye angle θ_a decreases, and there is a marked increase of μ_{le} from the padeye to the soil
475 surface (Figure 14(b)).

476 The values of μ_{le} derived from the proposed method are compared with the CEL results of the
477 F/Q in Figure 15 for cases of w_c = 0 and 1.5 kN/m. Note that segments in the vicinity of the
478 mudline were not considered in the analysis because the shallow part of the chain only
479 contributes a very small proportion of the overall resistance. Despite the fluctuations of the CEL
480 results, the overall predictions by Eqs. (9) and (10) agree well with the CEL results.

481 The above approach can also be used to calculate the average operative coefficient of the
482 friction μ_{op}^{mod} assuming normal resistance is fully mobilized ($Q = Q_{u,\,deep} = 19 d_b s_u$):

483
$$\mu_{op}^{\text{mod}} = \frac{\int_{z_a}^{0} \mu_{le} Q_u}{\int_{z_a}^{0} Q_u} \tag{11}$$

484 This was further examined by comparing the predictions of T_a/T_m calculated by Eq.(3) adopting
485 μ_{op}^{mod} and constant μ_{op} of 0.07 with the CEL results during the tensioning process as shown in
486 Figure 16. The tension ratio calculated with μ_{op}^{mod} shows an increase from 0.91 when θ_a = 75°
487 to just under 0.98 at when θ_a = 35°. Despite fluctuations of the CEL results, the T_a/T_m values
488 derived from μ_{op}^{mod} show better agreement with the numerical results than the simple and
489 constant μ_{op} = 0.07, particularly for small chain angles. This demonstrates the feasibility of the
490 proposed method for the calculation of the equivalent frictional coefficient of the embedded
491 chain.

CONCLUSIONS

A series of large deformation finite element analyses using the CEL approach were conducted to investigate the interaction between chain elements and the soil during different displacement trajectories and also the global system response of a catenary anchor chain cutting through soil. The results provide new insight into the response of an anchor chain system, in particular the operative axial 'friction' along the chain. A new design method is proposed for predicting tension and angle along the inverse catenary of an embedded anchor chain.

The CEL results of the configuration of the embedded chain and the tension at the padeye showed good agreement with analytical predictions, implying the suitability of assuming that normal soil resistance is fully mobilized when performing design calculations (as previously suggested by Neubecker and Randolph (1995b)). However, the CEL results showed significantly less tension attenuation from the mudline to the padeye of the embedded chain compared to previously published design approaches. This was shown to be due to the low proportion of the potential frictional capacity that is mobilized over the embedded chain during chain cutting. Partial mobilization of the frictional resistance was shown to result from interaction between the normal and frictional soil resistances as the embedded chain cuts through the soil, with almost full normal resistance and thus low frictional resistance being mobilized through most of the embedded part of chain governed by the stationary padeye condition. Consequently, the local mobilized coefficient of friction was shown to decrease significantly with increasing depth. The global 'operative' coefficient of friction, taking account of increasing shear strength with depth, is weighted towards the chain response at depth and hence is much lower than the nominal potential friction coefficient.

Equations for yield loci for the embedded chain were obtained from the numerical results and normality was demonstrated for the embedded chain sections. This allowed development of a new method for calculating the local equivalent coefficient of friction (i.e. F/Q) at every point

along the chain, based on the yield locus and the chain configuration, and hence the incremental displacement trajectories at each point. A formulation was also developed to estimate the global operative coefficient of friction acting along the chain, facilitating more accurate calculation of the tension variation along the embedded anchor chain. The resulting analytical approach showed good agreement with the CEL results locally and globally, confirming the potential for the approach for design of mooring systems with embedded anchor padeyes.

ACKNOWLEDGEMENTS

This work forms part of the activities of the Centre for Offshore Foundation Systems. Established in 1997 under the Australian Research Council's Special Research Centres Program and currently supported as a node of the Australian Research Council's Centre of Excellence for Geotechnical Science and Engineering (ARC grant CE110001009), and through the Fugro Chair in Geotechnics, the Lloyd's Register Foundation Chair and Centre of Excellence in Offshore Foundations and the Shell EMI Chair in Offshore Engineering. The first author is supported with a Fugro PhD Scholarship, the second author is supported by the National Natural Science Foundation of China (No. 51890915) and the fifth author is supported as the Fugro Chair in Geotechnics. All the support above is gratefully acknowledged.

REFERENCES

Aubeny, C. P., Han, S. W., and Murff, J. D. (2003). "Inclined load capacity of suction caissons." *International Journal for Numerical and Analytical Methods in Geomechanics*, 27(14), 1235-1254.

Bhattacharjee, S., Majhi, S. M., Smith, D., and Garrity, R. (2014). "Serpentina FPSO Mooring Integrity Issues and System Replacement: Unique Fast Track Approach." In *Proc., Offshore Technology Conference*, Offshore Technology Conference.

Bransby, M. F., and Randolph, M. F. (1998). "Combined loading of skirted foundations." *Géotechnique*, 48(5), 637-655.

Colliat, J.-L., Safinus, S., Boylan, N., and Schroeder, K. (2018). "Formation and Development of Seabed Trenching from Subsea Inspection Data of Deepwater Gulf of Guinea Moorings." In *Proc., Offshore Technology Conference*, Offshore Technology Conference.

Dassault Systèmes (2014). *ABAQUS 6.14 Analysis User's Manual*, Simulia Corp, Providence, RI, USA.

Degenkamp, G., and Dutta, A. (1989). "Soil resistances to embedded anchor chain in soft clay." *Journal of Geotechnical Engineering*, 115(10), 1420-1438.

Dutta, A., and Degenkamp, G. (1989). "Behaviour of embedded mooring chains in clay during chain tensioning." In *Proc., Offshore Technology Conference*, Offshore Technology Conference.

Ehlers, C. J., Chen, J., Roberts, H. H., and Lee, Y. C. (2005). "The origin of near-seafloor crust zones in deepwater." In *Proc., Proc. Int. Symp. on Frontiers in Offshore Geotechnics: ISFOG*, 927-934.

Frankenmolen, S. F., White, D. J., and O'Loughlin, C. D. (2016). "Chain-Soil Interaction in Carbonate Sand." In *Proc., Offshore Technology Conference*, Offshore Technology Conference.

Gault, J. A., and Cox, W. R. (1974). "Method for predicting geometry and load distribution in an anchor chain from a single point mooring buoy to a buried anchorage." In *Proc., Offshore Technology Conference*, Offshore Technology Conference.

Han, C., and Liu, J. (2017). "A modified method to estimate chain inverse catenary profile in clay based on chain equation and chain yield envelope." *Applied Ocean Research*, 68, 142-153.

Kim, Y., Hossain, M. S., and Wang, D. (2015). "Dynamically Installed Anchors: Performance of embedded mooring chain profile in clay." *Frontiers in Offshore Geotechnics III*, Meyer, ed., Taylor & Francis Group, London, 881-886.

Neubecker, S., and Randolph, M. (1995a). "Performance of embedded anchor chains and consequences for anchor design." In *Proc., Offshore Technology Conference*, Offshore Technology Conference.

Neubecker, S., and Randolph, M. (1995b). "Profile and frictional capacity of embedded anchor chains." *Journal of geotechnical engineering*, 121(11), 797-803.

Neubecker, S., and Randolph, M. (1996). "The performance of drag anchor and chain systems in cohesive soil." *Marine georesources & geotechnology*, 14(2), 77-96.

O'Neill, M. P., Bransby, M. F., and Randolph, M. F. (2003). "Drag anchor fluke soil interaction in clays." *Canadian Geotechnical Journal*, 40(1), 78-94.

Randolph, M., and Gourvenec, S. (2011). *Offshore geotechnical engineering*, CRC Press.

Reese, L. C. (1973). "A design method for an anchor pile in a mooring system." In *Proc., Offshore Technology Conference*, Offshore Technology Conference.

Rocha, M., Schnaid, F., Rocha, C., and Amaral, C. (2016). "Inverse catenary load attenuation along embedded ground chain of mooring lines." *Ocean Engineering*, 122, 215-226.

Vivatrat, V., Valent, P. J., and Ponterio, A. A. (1982). "The influence of chain friction on anchor pile design." In *Proc., Offshore Technology Conference*, Offshore Technology Conference.

Wang, D., Bienen, B., Nazem, M., Tian, Y., Zheng, J., Pucker, T., and Randolph, M. F. (2015). "Large deformation finite element analyses in geotechnical engineering." *Computers and Geotechnics*, 65, 104-114.

Yen, B. C., and Tofani, G. D. (1984). "Soil resistance to stud link chain." In *Proc., Offshore Technology Conference*, Offshore Technology Conference.

Zhao, Y., and Liu, H. (2013). "Large deformation finite element analysis of the anchor line embedded in seabed soils." In *Proc., ASME 2013 32nd International Conference on Ocean, Offshore and Arctic Engineering*, American Society of Mechanical Engineers, V006T010A024-V006T010A024.

Zhao, Y., and Liu, H. (2014). "Numerical simulation of drag anchor installation by a large deformation finite element technique." In *Proc., ASME 2014 33rd International Conference on Ocean, Offshore and Arctic Engineering*, American Society of Mechanical Engineers, V003T010A011-V003T010A011.

Zhao, Y., and Liu, H. (2016). "Numerical implementation of the installation/mooring line and application to analyzing comprehensive anchor behaviors." *Applied Ocean Research*, 54, 101-114.

Figure captions

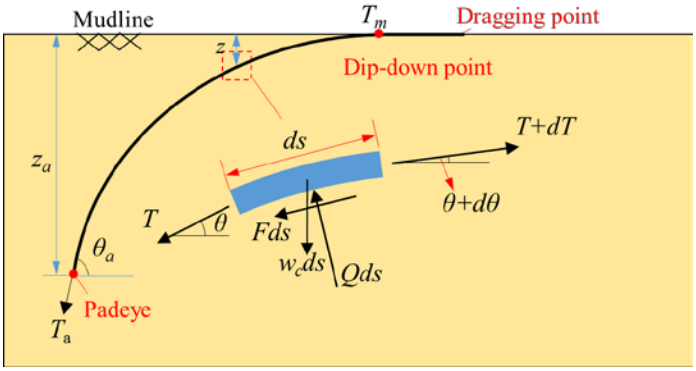

Figure 1. A global embedded chain and the mechanical equilibrium of a chain element

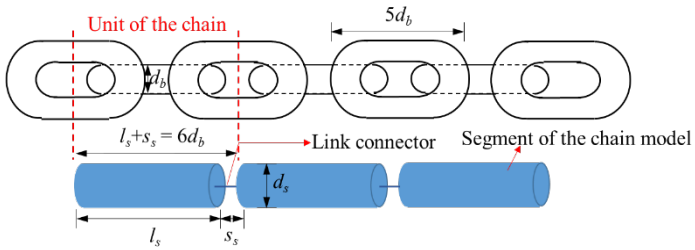

(a) Chain model corresponding to the $5d_b$ studless chain

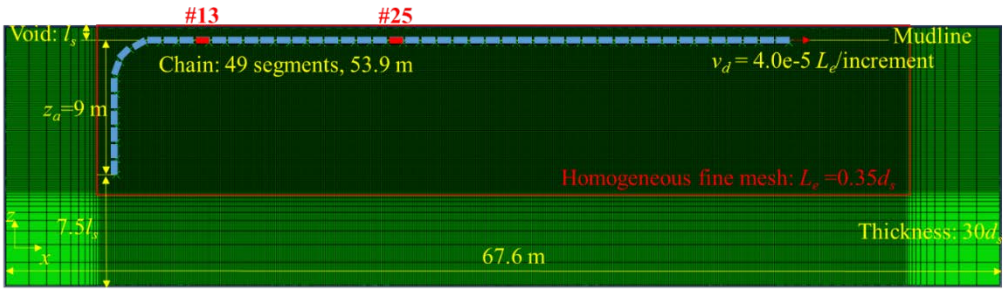

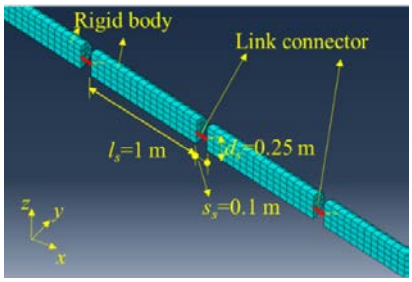

(b) FE model setup

Figure 2. CEL modelling of the embedded chain

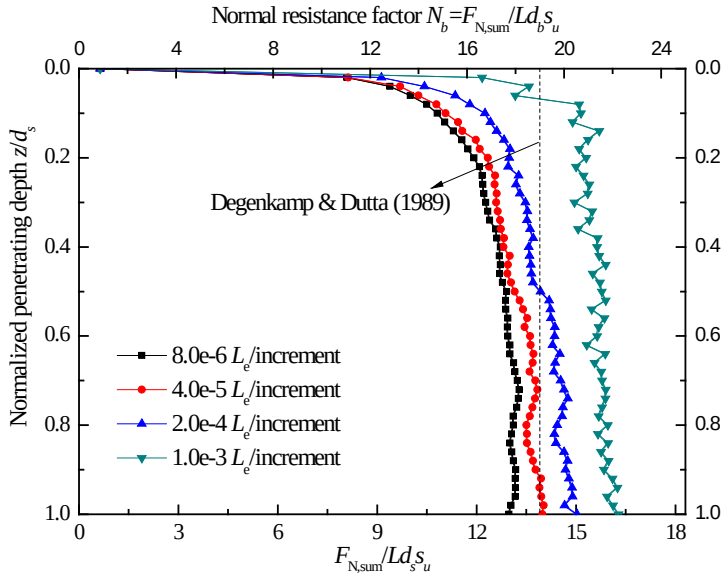

627

628 (a) Normal

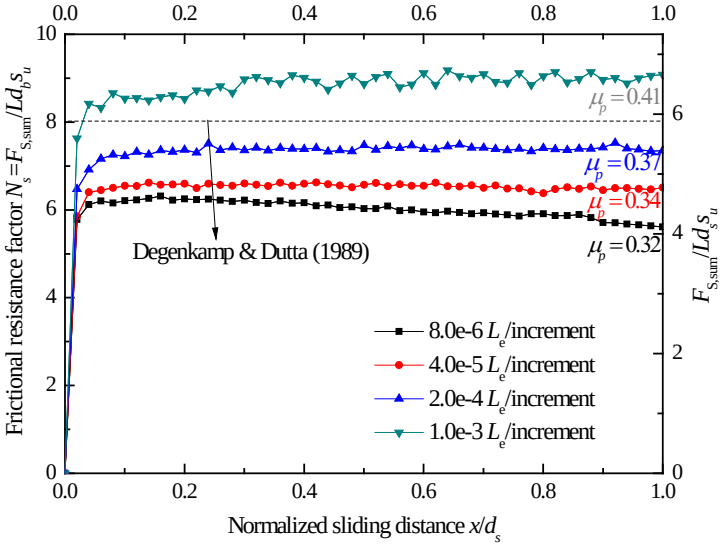

629

630 (b) Frictional

631 Figure 3. Capacities of the embedded chain model with different penetrating/sliding velocities

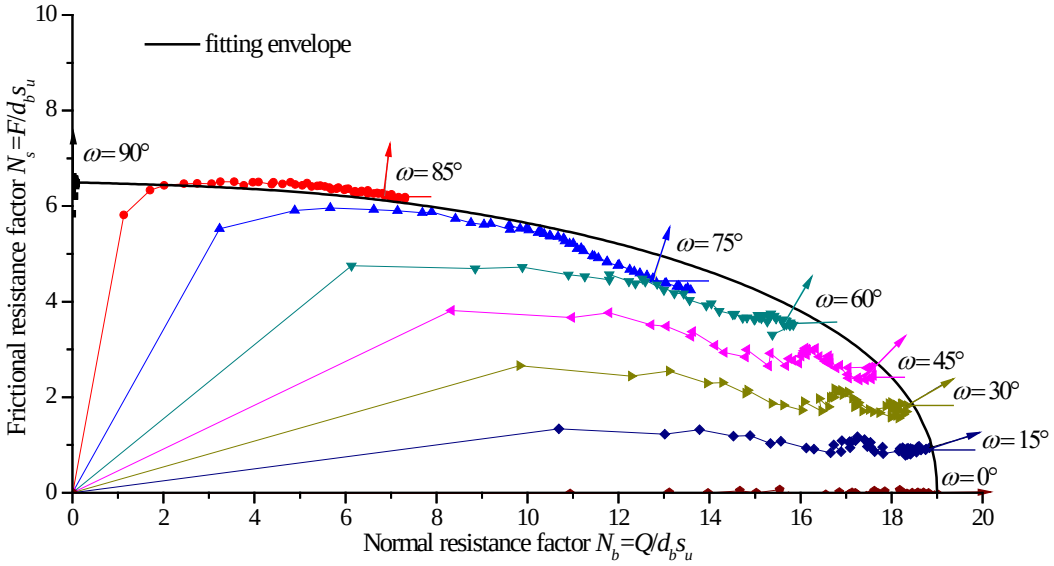

(a) Deep embedment ($18d_s$)

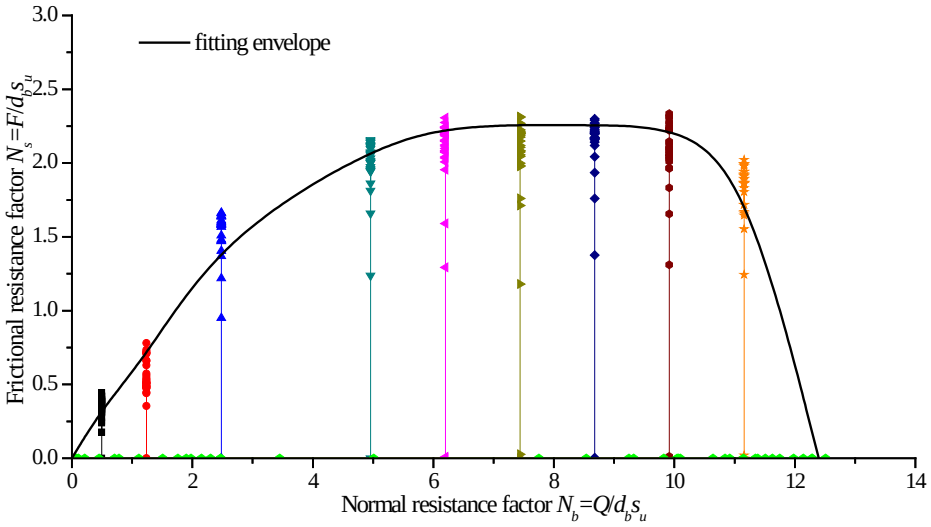

(b) Surficial

Figure 4. Probe testing results of the weightless chain model

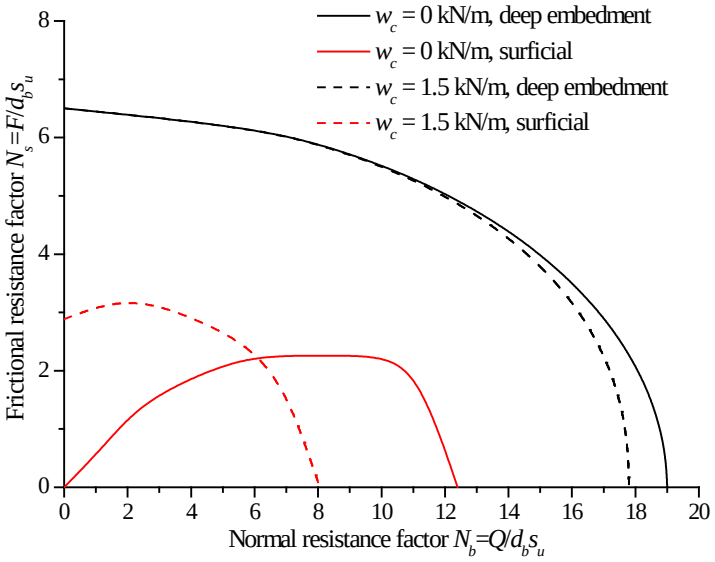

637

638 Figure 5. Yield loci of the embedded chain model

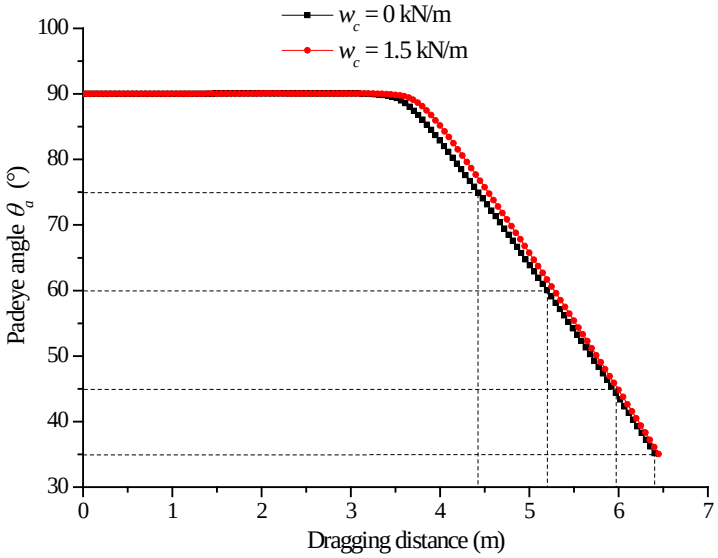

(a) Padeye angle

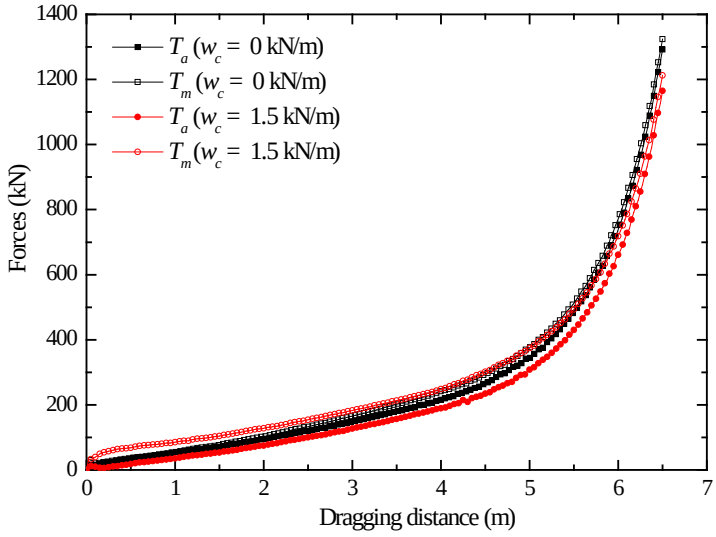

(b) Mudline and padeye tensions

Figure 6. Development of padeye angle and forces of the full chain system during tensioning

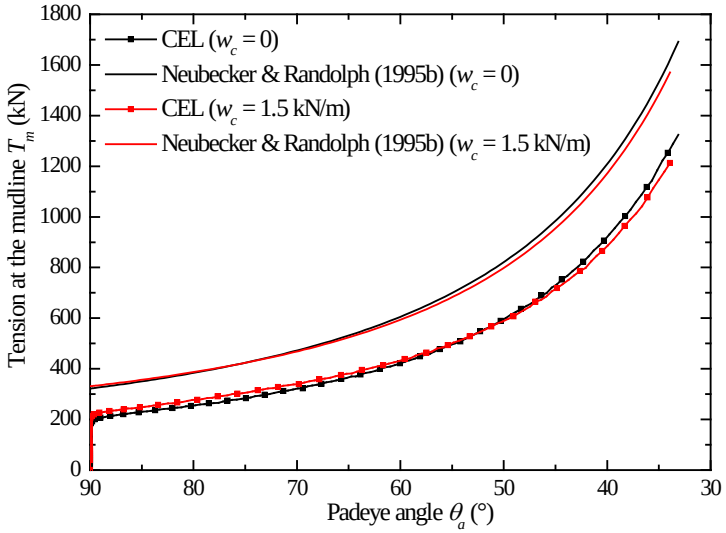

644

645 (a) Mudline tension

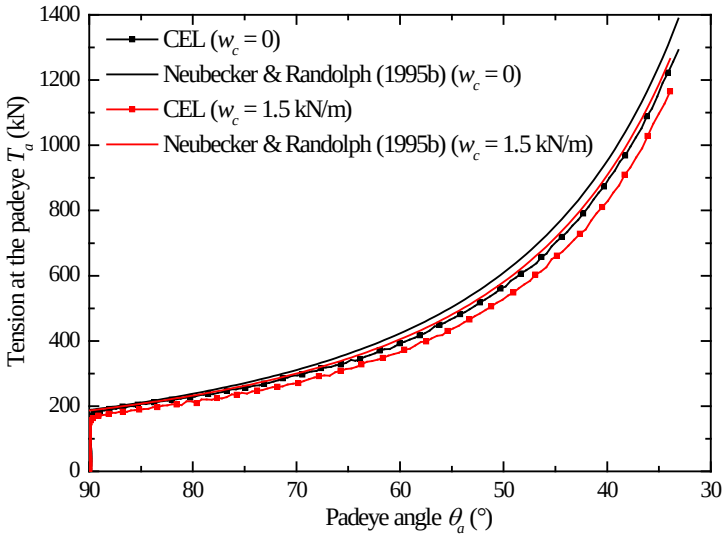

646

647 (b) Padeye tensions

648 Figure 7. Comparison of tension-padeye angle relationships

649

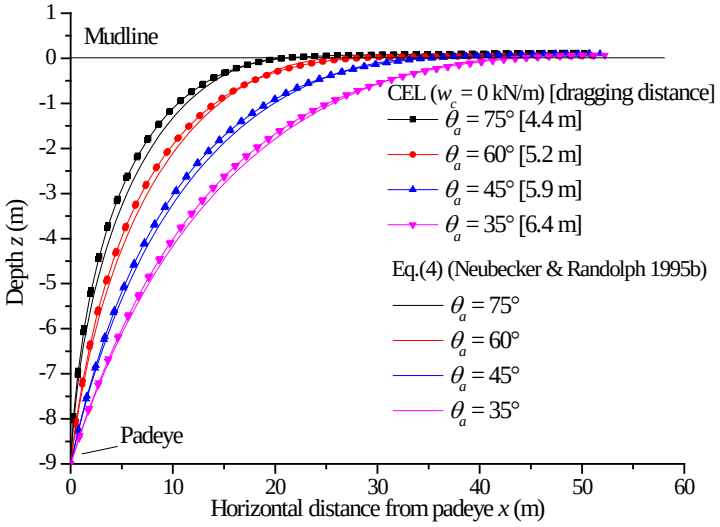

650

651 (a) w_c = 0 kN/m

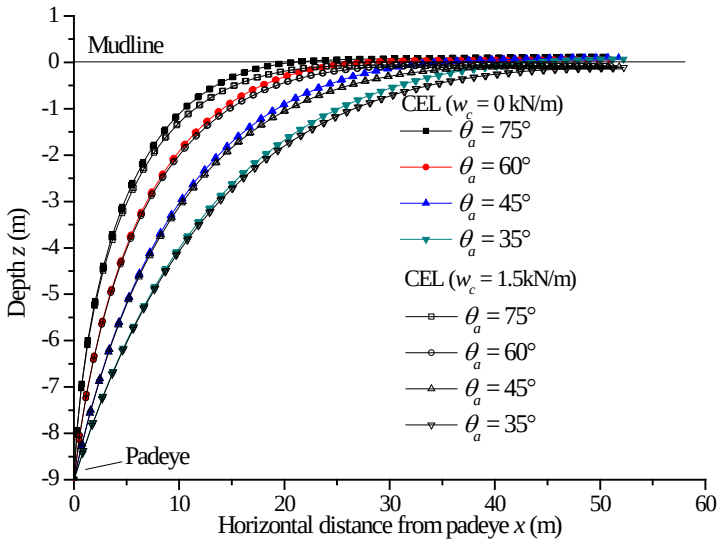

652

653 (b) Chain weight effect

654 Figure 8. Configurations of the embedded chain for selected chain inclination angles at the

655 padeye during tensioning

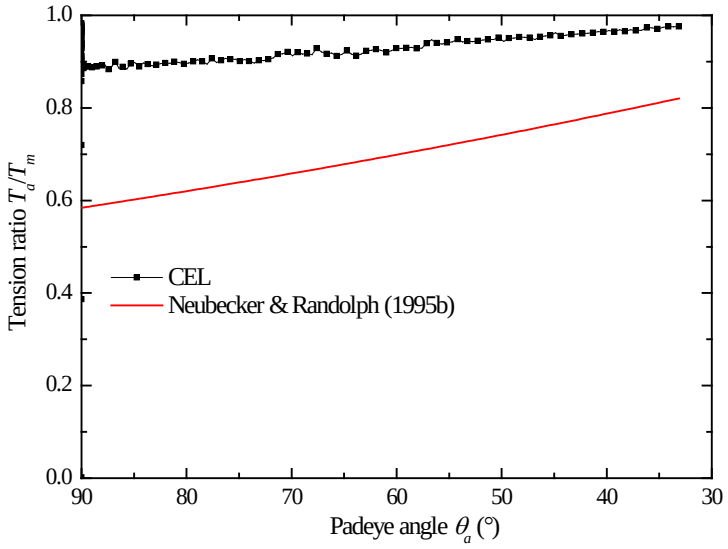

(a) Tension ratio during tensioning (w_c = 0)

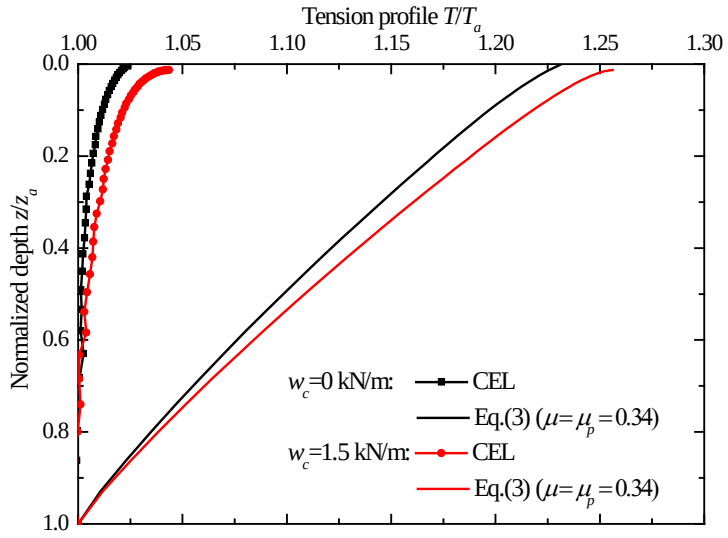

(b) Tension conditions in the chain at the padeye angle of 35°

Figure 9. Tension in the chain

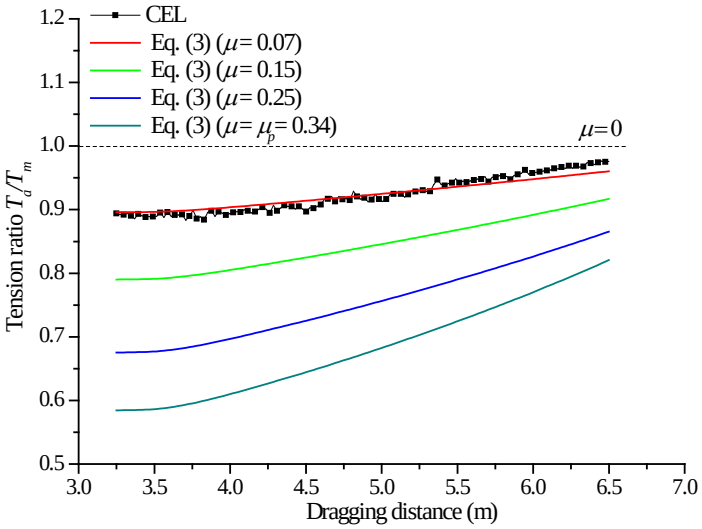

Figure 10. Effect of operative coefficient of friction of the embedded chain on the tension ratio

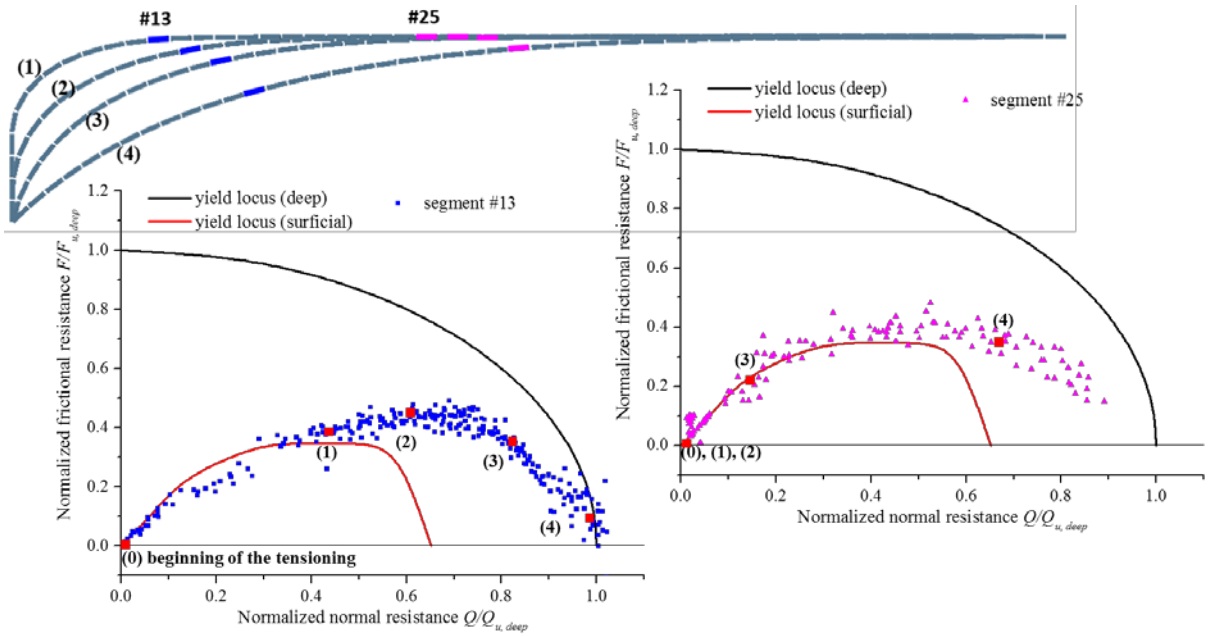

Figure 11. Evolution of the soil resistances to representative chain segments during tensioning

666

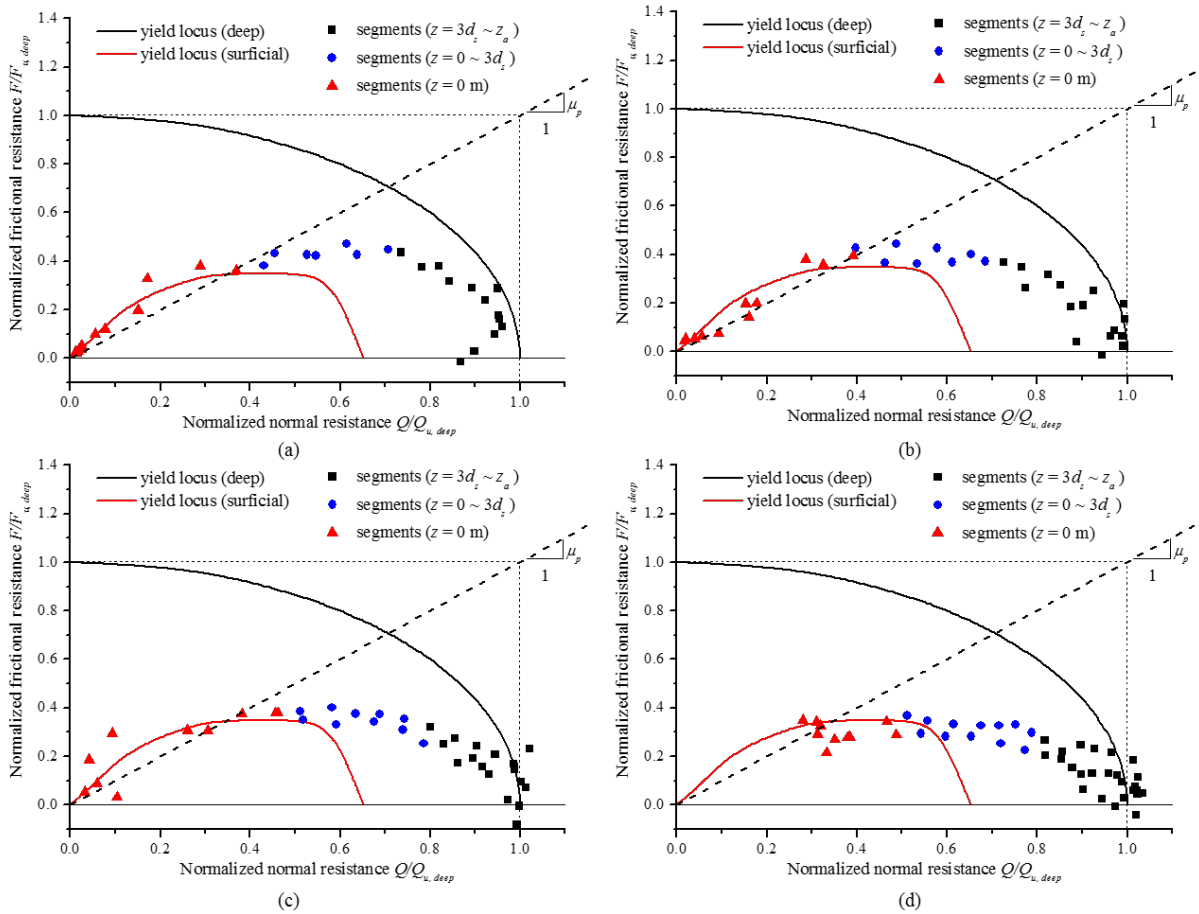

667

668 Figure 12. Distributions of the soil resistances of the embedded chain with the yield loci:

669 (a) $\theta_a = 75^\circ$ (b) $\theta_a = 60^\circ$ (c) $\theta_a = 45^\circ$ (d) $\theta_a = 35^\circ$

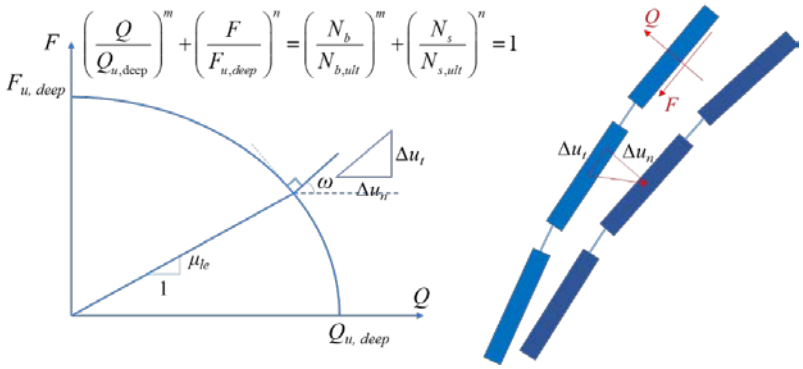

Figure 13. Schematic of the yield locus and the plastic potential function

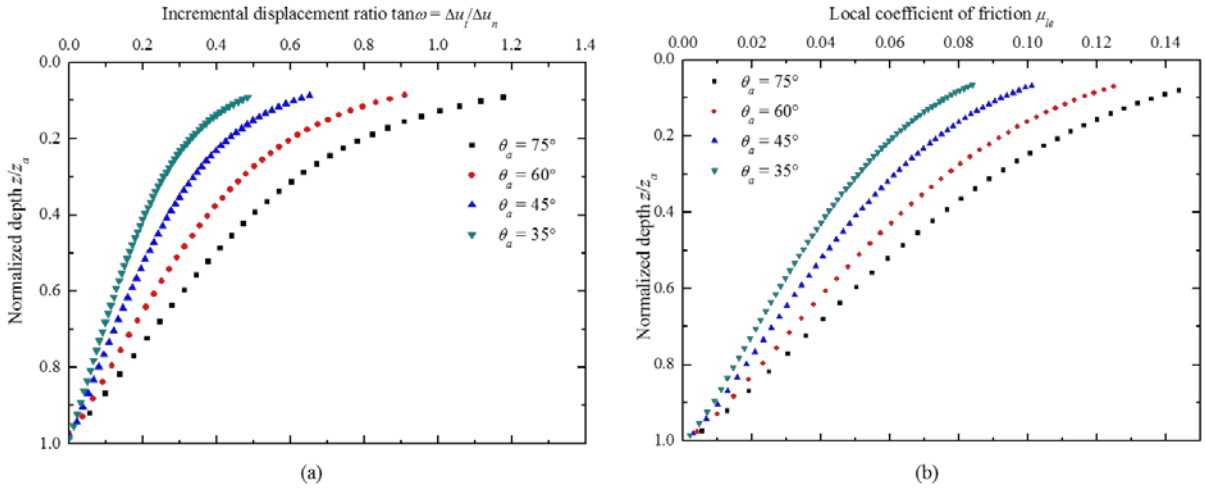

673

674 Figure 14. Example of the calculation for the local equivalent coefficient of friction based on

675 the configurations solved by the Neubecker & Randolph solution: (a) Incremental

676 displacement ratio; (b) Local equivalent coefficient of friction

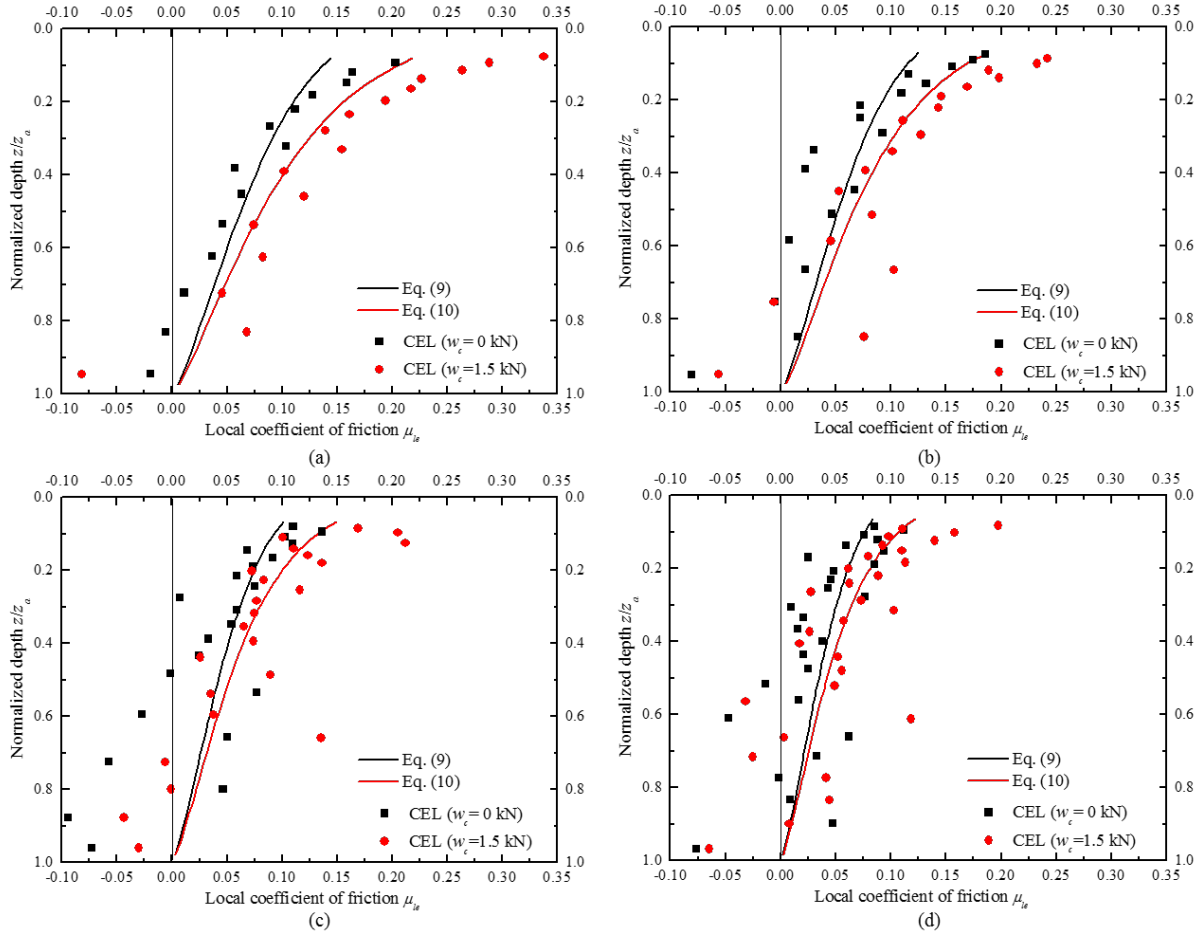

Figure 15. Distribution of the local equivalent coefficient of friction of the chain with different padeye angles: (a) θ_a = 75° (b) θ_a = 60° (c) θ_a = 45° (d) θ_a = 35°

680

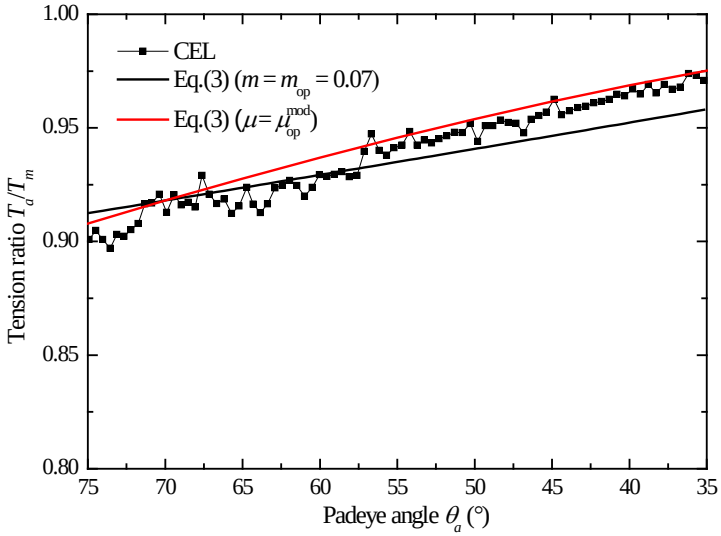

681

682 Figure 16. Tension ratio calculated with modified operative frictional coefficient